Parameterization of Centimeter-Scale Sea Ice Surface Roughness Using Terrestrial LiDAR

Article *in* IEEE Transactions on Geoscience and Remote Sensing · March 2015

DOI: 10.1109/TGRS.2014.2336833

4 authors, including:

Jack Landy
University of Bristol
30 PUBLICATIONS **226** CITATIONS

SEE PROFILE

Dustin Isleifson
University of Manitoba
32 PUBLICATIONS **187** CITATIONS

SEE PROFILE

Alexander S. Komarov
Environment Canada
38 PUBLICATIONS **290** CITATIONS

SEE PROFILE

Parameterization of Centimeter-Scale Sea Ice Surface Roughness Using Terrestrial LiDAR

Jack C. Landy, Dustin Isleifson, Alexander S. Komarov, *Student Member, IEEE*, and David G. Barber

***Abstract*—Microwave scattering from sea ice is partially controlled by the ice surface roughness. In this paper, we propose a technique for calculating 2-D centimeter-scale surface roughness parameters, including the rms height, correlation length, and form of autocorrelation function, from 3-D terrestrial light detection and ranging data. We demonstrate that a single scale of roughness can be extracted from complex sea ice surfaces, incorporating multiple scales of topography, after sophisticated 2-D detrending, and calculate roughness parameters for a wide range of artificial and natural sea ice surface types. The 2-D technique is shown to be considerably more precise than standard 1-D profiling techniques and can therefore characterize surface roughness as a stationary single-scale process, which a 1-D technique typically cannot do. Sea ice surfaces are generally found to have strongly anisotropic correlation lengths, indicating that microwave scattering models for sea ice should include surface spectra that vary as a function of the azimuthal angle of incident radiation. However, our results demonstrate that there is no fundamental relationship between the rms height and correlation length for sea ice surfaces if the sampling area is above a threshold minimum size.**

***Index Terms*—Geophysical measurements, ice surface, laser applications, measurement by laser beam, radar scattering, sea ice, surface roughness, surface topography.**

I. Introduction

ACTIVE microwave remote sensors can provide valuable insight into the geothermophysical conditions of snow-covered sea ice [1]. Radar scattering signatures are linked to geophysical parameters through microwave scattering models [2], which can include separate formulations for surface and volume scattering within layered snow and ice media [3]. Modeled backscatter is particularly sensitive to variations in roughness at the air–snow or snow–ice interface, when the dielectric contrast between layers is high. Therefore, it is important that the statistical parameters characterizing surface roughness correctly describe the physical properties of a rough interface. However, conventional techniques for *in situ* measurement and analysis of surface roughness are limited [4], [5], and incorrect values for the surface roughness parameters introduce significant bias into modeled backscatter [5].

Surface roughness is generally treated as a stationary single-scale random process, describing height deviations from a reference level, in microwave scattering models [4]. In reality, natural surfaces are characterized by an aggregate of several superimposed scales of roughness, created by various physical forcing mechanisms. Sea ice comprises three general length scales: macro ($>$ 100 m; level or ridged ice), meso (0.1–100 m; snow drifts), and micro ($<$ 0.1 m; frost flowers, snow grains, or bare ice) [6], [7]; roughness at each of these scales is a product of dynamic and/or thermodynamic forcing. For instance, strong winds can cause ice ridging, snow drift redistribution, and snow or ice surface scouring, potentially modifying surface roughness at all three scales.

It is common practice to remove or "detrend" large-scale topography from a natural surface and consider micro- and meso-/macroscales of roughness separately in scattering models [4]. The single-scale assumption is then valid for small-scale roughness, and large-scale topography can be characterized as a distribution of surface slopes (or inclination angles) on which the small-scale roughness is superimposed. In other words, rough surfaces are tilted toward or away from the incident radiation beam, and the reference level for characterizing small-scale roughness is represented by large-scale topographic trend.

The goal of this study is to develop a method for calculating surface roughness parameters from 3-D elevation data acquired with a terrestrial light detection and ranging (LiDAR) instrument. In Section II, we review the surface roughness theory and the conventional techniques for measuring surface roughness. In Section III, we outline a procedure for collecting and preprocessing the LiDAR data and introduce two 2-D detrending algorithms for removing large-scale topography. In Section IV, we present roughness parameters calculated from natural and artificial snow and sea ice surfaces, in both one and two dimensions, and evaluate the sensitivity of calculated roughness parameters to variations in the sampling approach. In Section V, we discuss potential sources of error in the LiDAR measurements and roughness parameters, and the implications of our results for microwave scattering from sea ice. Finally, in Section VI, we conclude.

II. Background

For a 2-D random rough surface, $\zeta(\boldsymbol{\rho}')$, with zero average value $\langle \zeta(\boldsymbol{\rho}') \rangle = 0$, where $\boldsymbol{\rho}' = \{x, y\}$ is a position vector in the horizontal plane [8]

$$\sigma^2 = \left\langle \zeta^2(\boldsymbol{\rho}') \right\rangle \tag{1}$$

Manuscript received October 8, 2013; revised March 7, 2014 and April 30, 2014; accepted June 16, 2014. This work was supported by a Canada Research Chair program grant to D. G. Barber and an Natural Sciences and Engineering Research Council CGS-D3 Scholarship to A. S. Komarov.

J. C. Landy and D. G. Barber are with the Centre for Earth Observation Science, University of Manitoba, Winnipeg, MB R3T 2N2, Canada.

D. Isleifson and A. S. Komarov are with the Department of Electrical and Computer Engineering, University of Manitoba, Winnipeg, MB R3T 5V6, Canada and also with the Centre for Earth Observation Science, University of Manitoba, Winnipeg, MB R3T 2N2, Canada.

Color versions of one or more of the figures in this paper are available online at http://ieeexplore.ieee.org.

Digital Object Identifier 10.1109/TGRS.2014.2336833

where σ is the root-mean-square (rms) roughness height. For a stationary random process, the normalized autocorrelation function is given by

$$C(\boldsymbol{\rho}) = \frac{\langle \zeta(\boldsymbol{\rho}+\boldsymbol{\rho}')\zeta(\boldsymbol{\rho}')\rangle}{\langle \zeta^2(\boldsymbol{\rho}')\rangle} \tag{2}$$

where $\boldsymbol{\rho}$ is the shift vector in the horizontal plane. The correlation length l is the absolute value of $\boldsymbol{\rho}$ for which $C(\boldsymbol{\rho}) = e^{-1}$. l can then be defined with respect to the azimuth angle φ as follows:

$$C\left(l(\varphi)\cos\varphi, l(\varphi)\sin\varphi\right) = e^{-1}. \tag{3}$$

The eccentricity of the surface correlation, a measure of the roughness isotropy, is

$$\epsilon_l = \sqrt{1 - \left(\frac{\min(l)}{\max(l)}\right)^2}. \tag{4}$$

Following the notation of [3], if l is independent of φ, i.e., the surface is isotropic, the exponential correlation function is given by

$$C(\boldsymbol{\rho}) = \exp\left(-\frac{\rho}{l}\right) \tag{5}$$

and the Gaussian correlation function is given by

$$C(\boldsymbol{\rho}) = \exp\left(-\frac{\rho^2}{l^2}\right). \tag{6}$$

A generalized power-law correlation function is therefore

$$C(\boldsymbol{\rho}) = exp\left[-\left(\frac{\rho}{l}\right)^n\right] \tag{7}$$

where $1 < n < 2$, so that the function converges to the exponential or Gaussian as n approaches 1 or 2, respectively.

Drinkwater [9] found that the rough surface of level undeformed ice was best described by exponential $C(\boldsymbol{\rho}')$ (hereafter referred to only as C), whereas deformed ice was best described by Gaussian C. It was assumed that the exponential function, which is characterized by smaller correlations at shorter lag distances than the Gaussian function, was identifying microscale roughness features over the undeformed ice that were not present over the deformed ice. However, a later study showed that rough surfaces from both level and deformed ice mostly conformed to exponential C [6], which suggests that the sampling interval used by Drinkwater to discretize roughness on the ice surface ($\sim$1 cm) may not have been small enough to properly characterize the measured correlation function [9].

The choice of the sampling interval (Δx) and the sampling extent (L) can have a profound effect on the derived roughness parameters. Several groups have used numerical methods to simulate the effect of sampling interval on roughness parameters. Ogilvy and Foster determined that a sampling interval of $0.1l$ is required to differentiate between exponential and Gaussian C [10], and a later study has shown that an interval of $0.2l$ is required to accurately calculate the correlation length [11]. Ulaby *et al.* suggested that the sampling interval should be no higher than 0.1 of the microwave observable wavelength (i.e., the wavelength at C-band is $\sim$5.5 cm, so the sampling interval should be no more than $\sim$5.5 mm) [12].

Numerous studies have also demonstrated that roughness parameters are dependent on sampling extent (the length of a profile or area of a surface) up to a limit $(L_{\min})$, approached asymptotically with increasing extent [6], [11], [13]. Below $L_{\min}$, the rms height and correlation length are underestimated because the measured profile fails to capture surface height extrema and cannot be assumed to be stationary [4], [5]. If the measured profile is not stationary, σ and l will change when shifted in space. Estimates for $L_{\min}$ from numerical simulations are not in agreement, however, with Oh and Kay [11] reporting that $L_{\min}$ should be at least $40l$ and $200l$ for the determination of σ and l with an error of $< 10\%$, respectively, and Nishimoto [13] reporting the same criteria as $240l$ and $458l$, respectively. Owing to the dependence of σ and l on L, attempts have been made to characterize rough surfaces using band-limited fractals, e.g., [6] and [14]. However, backscatter models typically require that surface roughness is treated as a single-scale process, so research into this area has not been widely pursued.

Field- or laboratory-based surface roughness measurements have generally been made along discrete 1-D profiles, using either contact or noncontact instruments. Detailed descriptions of the methods used to collect surface roughness data over snow and sea ice are rare, so we include studies targeting, for example, soil or outcrop roughness, as we review these techniques. Contact instruments include the stylus profilometer [6], [15], meshboard [16], and pin profiler [17]. The key disadvantage of a contact instrument is that it can interfere with the physical properties of the surface, especially if the surface comprises fragile structures, such as newly fallen snow. Moreover, these instruments typically also have limited horizontal resolution and extent, e.g., standard pin profilers include pins with 1-cm spacing [18] and both these and stylus profilometers are generally limited to 1-m long transects [6]. Noncontact techniques include photographing a surface against a background grid [7], [19] and, most commonly, laser profiling [9], [20], [21]. These instruments do not disturb the surface and can generally sample at spatial resolutions of < 1 cm, but only the laser profiler can measure transects with a length greater than $\sim$1 m.

The vast majority of these techniques, both contact and noncontact, are vulnerable to errors introduced by inadequate sampling interval and/or extent [20]. However, a fundamental limitation of all profiling techniques is that 1-D statistics are assumed to represent 2-D surface properties, which is not always the case [20]. Individual profiles across a surface may not be translationally invariant (causing roughness statistics to vary considerably between adjacent profiles), and consequently, the surface cannot be assumed to be stationary [4]. One-dimensional profiles also fail to identify anisotropy in surface roughness which, for example, has previously been measured over snow on sea ice [6].

Therefore, a few groups have started to experiment with techniques such as photogrammetry [18], [22] and dual-axis laser scanning (or LiDAR) [17], [18], [23], [24] for characterizing surface roughness in two dimensions. However, the methods for analyzing surface roughness from the 3-D elevation data obtained with these instruments vary. For instance, Bryant *et al.*

TABLE I
PROPERTIES OF 40 LiDAR SECTIONS, COLLECTED OVER VARIOUS TYPES OF SEA ICE AT DIFFERENT STAGES OF EVOLUTION, USED IN THE STUDY TO INVESTIGATE SNOW AND ICE SURFACE ROUGHNESS. "THICKNESS" REFERS TO THE APPROXIMATE MEAN SEA ICE THICKNESS AT THE TIME OF ACQUISITION. "STAGE" AND "HOUR" REFER TO THE STAGE OF ICE DEVELOPMENT AND NUMBER OF HOURS SINCE INITIAL ICE FORMATION, RESPECTIVELY. "NO. SECTIONS" REFERS TO THE NUMBER OF INDIVIDUAL LiDAR SECTIONS OBTAINED FOR AN ICE TYPE OR STAGE OF EVOLUTION

Snow/Ice Type	Code	Location	Thickness [cm]	Stage (Hour)	No. Sections
Bare Congelation Ice	BI	SERF	7		3
Refrozen Slush	RS	SERF	8		3
Pancake Ice	PI	SERF	5	I (15)	3
			9	II (37)	3
			11	III (61)	3
Frost Flowers	FF	SERF	0.5	I (9)	4
			1	II (11)	3
			2	III (16)	3
			5	IV (64)	4
Wet Snow	S	Resolute*	100		1
Superimposed Ice	SI	Resolute*	100		1
First-Year White Ice	FYI	Resolute*	100		5
Multi-Year White Ice 1	MYI1	Beaufort Sea**	430		2
Multi-Year White Ice 2	MYI2	Beaufort Sea***	360		2

*Approx. Lat/Lon: * 74.73 N 95.58 W, **74.86 N 128.30 W, ***75.03 N 128.98 W.*

[17] calculated σ as the mean of 20 (or more) 1-m profiles extracted from LiDAR elevation models, whereas Jester and Klik [18] calculated σ as the overall rms roughness height of a 2-D surface grid, obtained with a downward-looking traversing laser scanner. These are preliminary studies, and to our knowledge, there has not yet been any research published on the extraction of complex roughness parameters, such as C and l, from 2-D LiDAR data.

It is not only the measurement technique but also the method for detrending surface roughness data that varies between studies. Many groups implicitly assume that surface height only varies in one direction, i.e., perpendicular to the principal plane, within the sampling extent. Therefore, data are detrended by fitting a mean line through a profile by ordinary least-squares regression (OLSR) and assessing surface roughness with respect to this local datum [6], [17], [21]. These regression lines can be fit through the entire profile or multiple smaller segments, e.g., [17]. Pollyea and Fairley [24] updated this approach by considering orthogonal distance regression planes, rather than OLSR planes, through 3-D LiDAR surface elevation data, which are robust to principal axis orientation. These techniques can introduce erroneous "jumps" between profiles or segments at the intersection between adjacent regression lines, over surfaces with high topographic relief [20]. Higher order polynomials have been used to detrend nonlinear topography from surface profiles [5], [20]. However, the natural surfaces of agricultural fields or sea ice, for example, rarely demonstrate topographic trends that can be described by linear or nonlinear functions. Moreover, in these circumstances, a high-pass filter based on the fast Fourier transform (FFT), which removes all spatial frequencies lower than a specified cutoff frequency from the topography, has proved to be more effective than linear or polynomial detrending techniques [20]. In any case, incorrect detrending introduces systematic bias into surface roughness statistics.

III. METHODS

A. Data Collection and Preprocessing

A Leica Scanstation C10 laser scanner was used to measure snow and sea ice surface roughness at an experimental ice tank facility [Sea-ice Environmental Research Facility (SERF)] on the University of Manitoba Campus (Winnipeg, MB, Canada) and at three locations in the Canadian High Arctic (Table I). The SERF is an outdoor pool containing artificial seawater that was used to grow various types of sea ice during the winters of 2012 and 2013. Because the laser scanner is highly sensitive to movement and vibrations, it cannot be mounted to a ship or drifting station and is therefore only a practical option for measuring surface roughness when ice is thick enough to support the weight of the scanner directly (above $\sim$20 cm). However, the SERF poolside provided a stable vantage point for scanning newly formed ice with a thickness of less than a centimeter. Surface roughness measurements were obtained from four types of sea ice grown in the SERF pool: 1) bare congelation ice; 2) refrozen slush, caused by seawater flooding bare ice; 3) pancake ice; and 4) frost flowers [Fig. 1(a)–(d)]. Ice physical properties depended on variations in environmental forcing mechanisms, such as temperature and wind speed at the air–pool interface, especially during the earliest stages of ice formation. For more information on the diverse processes contributing to sea ice formation and growth, see [25].

Surface roughness measurements were obtained in the field by mounting the laser scanner directly on natural sea ice and sampling adjacent areas. Three field locations were selected, including the following: landfast seasonal (or "first-year") sea ice in Resolute Passage, Nunavut, sampled in the early melt season during June 2012, and two perennial (or "multiyear") sea ice floes in the Beaufort Sea, sampled late in the melt season during August 2011 (Table I). In Resolute Passage, we

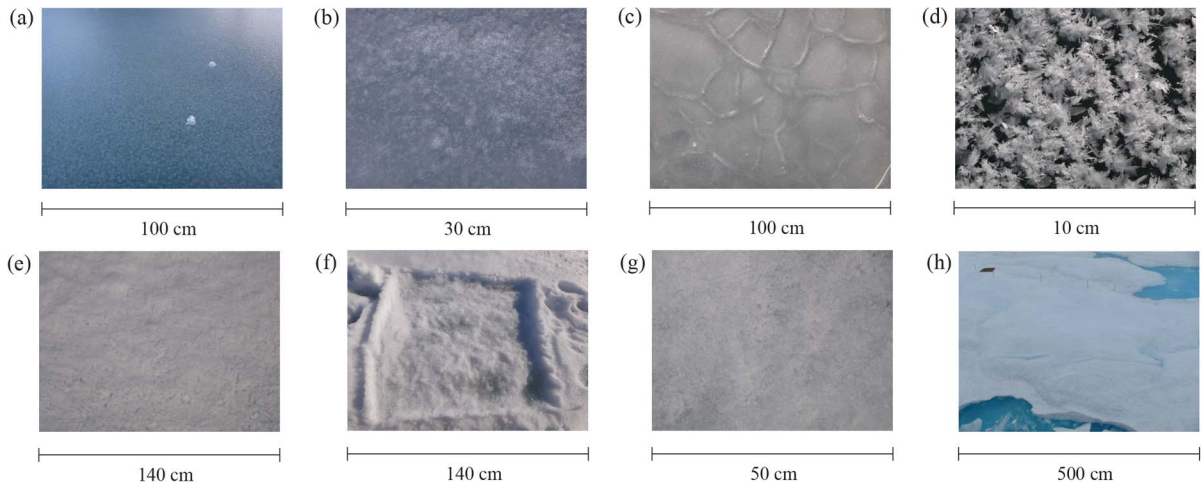

Fig. 1. Photographs of sea ice surfaces measured for roughness, including the following: (a) bare congelation ice, (b) refrozen slush, (c) pancake ice (at stage II, hour 38), (d) frost flowers (at stage III, hour 16), (e) wet snow on FYI, (f) superimposed ice cleared of the snow in photograph (e), (g) drained white ice surface on FYI, and (h) drained white ice surface on MYI. Approximate scales are given under each photograph.

first measured the roughness of the wet snowpack surface on June 9 [Fig. 1(e)] and then carefully cleared the snow to expose and sample a layer of superimposed ice [26] at the snow–ice interface [Fig. 1(f)]. After the snow cover melted completely, we measured the roughness of drained white ice [27] at the sea ice surface on June 19 [Fig. 1(g)]. We could only measure the roughness of white ice hummocks on multiyear sea ice in the Beaufort Sea [Fig. 1(h)], as the snowpack had melted long before we sampled in August.

The experimental setup was kept consistent between locations to ensure that results from the ice tank and field sites were comparable. Before sampling, the instrument was heated in a custom-built case to an operational temperature above 0 °C and then mounted on a level tripod. At the ice tank, the scanner and tripod were set up on a scaffold next to the pool, whereas at the field sites, they were set up on a custom-made platform directly on the ice. In both situations, the scanning origin was elevated to a height of 2.5–3 m above the target surface. The maximum range of the target surface from the scanner was consistently ∼10 m.

The Scanstation C10 is a discrete-pulse laser scanner that emits pulses of energy (532 nm wavelength) at a pulse repetition frequency of up to 50 kHz. It subsequently records the time-of-flight for each pulse to be reflected by objects in the target area and return to the scanner, thereby mapping the target in three dimensions. However, the snow and ice surfaces of interest in this study are not entirely opaque to the green light of Leica C10 but rather reflect by backscattering from a transparent media [28]. The laser may penetrate into the snow or ice for several millimeters, and multipath interactions will then spread the pulse return in time. The scanner computes the range from the first pulse return that has a backscattering intensity above an instrument-defined threshold. The method presented herein makes the fundamental assumption that the main source of the backscatter is from the surface of the medium, so the first valid return must generally be from surface rather than volume scattering. This assumption is supported by measurements of the reflectance and polarization of light from sea ice and by empirical experiments which are outlined in the following discussion. Past observations have demonstrated that green light which is reflected from a variety of ice types (including glazed melting snow, melting white ice, blue ice, bare congelation ice, and pancake ice), at a low incidence angle, is strongly polarized [29], [30]. This implies a substantial contribution from specular reflection in the direction of the light source [29]. The small amount of light which experiences volume scattering within the upper portion of the ice would be backscattered approximately uniformly over the hemisphere. Therefore, the returning laser pulse would include a strong defined front from surface backscatter and a long undefined tail from volume backscatter. The sensor would routinely compute a ranging estimate from the time-of-flight of the pulse front.

The minimum sampling interval of the scanner depends on the range of the target R, the inclination of the target surface with respect to the scanning origin θ, and the beam divergence of the laser δ. If the laser footprint diameter D_f is small compared to R [31]

$$D_f = 2R\tan\left(\frac{\delta}{2}\right). \tag{8}$$

The cross section of the laser beam's power distribution is Gaussian, and therefore, it is beneficial that the angular sampling interval of the scanner Δ is smaller than δ to yield a higher Nyquist frequency. Licthi and Jamtsho [32] have demonstrated that the optimal angular sampling interval $\Delta_{\text{opt}} = 0.859\delta$. Using this criteria, the optimal horizontal sampling interval of the C10 scanner x_{opt} is 2.06 mm at a range of 10 m. However, along the track of the laser beam, D_f becomes elongated if $\theta > 0$, and in our scans, θ ranged from approximately 45° to 70°. Along-track $D_{f_{\text{along}}}$ is given by [31]

$$D_{f_{\text{along}}} = \frac{2R\sin\left(\frac{\delta}{2}\right)\left[\cos(\theta)+\sin(\theta)\tan\left(\theta+\frac{\delta}{2}\right)\right]}{\cos\left(-\frac{\delta}{2}\right)}. \tag{9}$$

$D_{f_{\text{along}}}$ is approximately 2 mm at a range of 5 m (when $D_{f_{\text{across}}}$ is 1.2 mm) and is approximately 8 mm at a range of 10 m (when $D_{f_{\text{across}}}$ is 2.1 mm). The optimal along-track sample spacing x_{opt} is therefore 1.7 mm at a range of 5 m and 6.8 mm at 10-m range, using the criteria of [32]. Consecutive samples may have

become slightly correlated in the along-track direction, which could have affected the isotropy of the roughness calculations (see Section V-A).

As a compromise between the theoretical optimal along- and across-track sample spacing, scanning area, scanning time, and sampling interval criteria of [10]–[12], the scanner was configured so that the spacing between points along- and across-track was 2 mm at the selected maximum range (typically around 10 m). Preliminary analysis of test scans showed that regular millimeter–centimeter-scale physical features of the sea ice surface could be observed with this spatial resolution. The time required to scan a single $\sim$25–50 m^2 target at this resolution ranged from 30 to 60 min. Reported values for the correlation length of Arctic sea ice are generally above 1 cm [33], so a sampling interval of at least 2 mm satisfies the requirements given previously for identifying the correlation length [11], in addition to the criteria of Ulaby [12].

The vertical precision of the instrument was tested by repeatedly scanning two different target surfaces, both of which were assumed to have an effective rms height σ_{eff} of zero. In other words, σ_{eff} is more than an order of magnitude lower than the range resolution of the laser scanner. The target was scanned at a similar range and inclination angle to the artificial and natural sea ice surfaces, to keep the ranging and pointing errors consistent. The first target was a smooth laminate office floor, and the second target was a thin sheet of smooth sea ice grown from artificial seawater and stored in a cold laboratory at -20 °C at the University of Manitoba. Three 1×1 m floor sections were each scanned three times, and between the nine samples, the average standard deviation in the elevation of points with respect to a fixed reference level through the floor was 0.8 ± 0.3 mm. The $\sim 1 \times 1$ m sheet of sea ice was scanned three times from different orientations, and the average standard deviation of points through the ice surface was 1.4 ± 0.2 mm. However, the sea ice sheet could not be kept entirely smooth, but it was rough to touch, and the measured error was overestimated by the presence of larger ice crystals which grew at the surface as the ice formed. Therefore, σ_{eff} was above zero for the sea ice sheet. Between the two experiments, we can estimate that the noise floor of our measurements—incorporating the ranging precision of the sensor and volume scattering within the upper portion of the sea ice cover—is around 1 mm.

After data collection was complete, several preprocessing steps were performed on the LiDAR point clouds in preparation for calculating surface roughness parameters. To ensure that roughness parameters were calculated from the same area of the SERF pool, each scan in a series was registered to an arbitrary coordinate system that was consistently maintained by locating a number of fixed reflective targets, mounted around the edge of the pool, while scanning. Select scans from both the SERF and field sites contained outlying points located well above or below the true pool surface, caused by laser reflections from precipitation or multipath errors [34]. These outliers were removed using in-house algorithms based on the morphological [35] and adaptive triangulated irregular network [36] filters. The two filters iteratively removed points from scans that were outside a minimum user-defined inclination angle and/or distance from an initial estimate of the terrain.

A number of individual square sections, with a width of 1 to 3 m, were then extracted from each scan (Table I), and finally, points were resampled to a regular grid made up of 2 mm $\times$ 2 mm cells using linear interpolation. We chose to use linear interpolation, rather than a more sophisticated method of interpolation, because the sampling interval between raw LiDAR points was at most 2 mm. Therefore, basic linear interpolation helped to retain most of the information from the original data while resampling to a grid with cells typically larger in width than the sampling interval of the raw data points.

B. Detrending Algorithms

We present two detrending algorithms that remove the underlying topography from natural surfaces, leaving a single scale of roughness. Both algorithms are 2-D, removing topographic trends from a surface in its original 2-D form, rather than from individual profiles across it. The first is a 2-D adaptation of the commonly used OLSR method, developed as a baseline for assessing the second algorithm, which uses 2-D FFT to separate different wavelengths of roughness from a surface.

1) OLSR Planes: The OLSR algorithm consists of a sequence of routines that perform the following: 1) segment the original surface grid into a regular grid of lower spatial resolution; 2) establish local reference levels within each low-resolution grid cell by fitting OLSR planes to subsections of the original surface; and 3) reconstruct the surface after removing local reference levels from each grid cell. By varying the cell size of the low resolution grid, the user can adjust the scale of roughness (or topography) removed from the original surface.

The local reference datum within each low resolution grid cell C_x is defined as the plane for which

$$z = \beta_0 + \beta_1 x + \beta_2 y \tag{10}$$

where x, y, and z are coordinates of cells in the original surface grid and β_0, β_1, and β_2 are plane coefficients. These coefficients are found using OLSR, which identifies a local reference plane that minimizes vertical cell-to-plane distances. Original surface grid cells are then projected onto a new reconstructed grid—which retains the same x and y coordinates—by translating grid heights in the z-dimension.

2) FFT Filter: The FFT-based algorithm consists of a sequence of routines that perform the following: 1) take the 2-D discrete Fourier transform (DFT) of the original surface grid; 2) identify and filter the frequencies of roughness below a specified cutoff frequency (f_c); and 3) reconstruct the surface using the inverse DFT. By varying the cutoff frequency, the user can again adjust the scale of roughness (or topography) removed from the original surface.

3) Identifying the Cutoff Frequency: While the OLSR and FFT-based algorithms are fairly simple to compute and operate, the challenge with both is to select an appropriate low-resolution grid cell size or cutoff frequency, respectively, so as to retain all frequencies of roughness that affect microwave backscatter but also remove all frequencies that do not affect backscatter and therefore introduce errors into calculated surface roughness parameters. Therefore, we attempted to characterize the full range of roughness scales associated with a

TABLE II
COMPILATION OF SURFACE ROUGHNESS PARAMETERS EXTRACTED FROM ARTIFICIAL SEA ICE. VALUES FOR EACH SURFACE ARE AVERAGES FROM MULTIPLE LiDAR SECTIONS (SEE TABLE I)

Code	σ [cm]	l [cm] (1-D)			l [cm] (2-D)	
		Mean & Std	Min	Max	Mean & Std	ϵ_l
BI	0.23	0.27 ± 0.46	0.09	5.01	0.19 ± 0.00	0.19
RS	0.25	2.14 ± 1.19	0.62	11.12	2.25 ± 0.26	0.69
PI-I	0.23	1.15 ± 0.82	0.14	6.83	1.27 ± 0.11	0.63
PI-II	0.19	1.20 ± 0.66	0.16	4.69	1.36 ± 0.11	0.61
PI-III	0.21	0.37 ± 0.39	0.12	5.27	0.27 ± 0.04	0.73
FF-I	0.13	0.71 ± 0.14	0.57	1.90	1.01 ± 0.32	0.90
FF-II	0.19	0.44 ± 0.23	0.17	2.91	0.70 ± 0.47	0.98
FF-III	0.26	0.59 ± 0.58	0.30	5.46	0.85 ± 0.50	0.93
FF-IV	0.21	1.28 ± 0.34	0.57	6.61	1.36 ± 0.34	0.86

TABLE III
VARIATION IN SURFACE ROUGHNESS PARAMETERS EXTRACTED FROM NATURAL SEA ICE AFTER DETRENDING USING THE FOLLOWING: 1) THE OLSR ALGORITHM WITH 1-m GRID CELLS (OLSR-1); 2) THE OLSR ALGORITHM WITH 0.25-m GRID CELLS (OLSR-0.25); AND 3) THE FFT-BASED ALGORITHM WITH A 0.25-m CUTOFF WAVELENGTH (FFT-0.25). VALUES FOR EACH SURFACE ARE AVERAGES FROM MULTIPLE LiDAR SECTIONS, WITH THE EXCEPTION OF S AND SI (SEE TABLE I)

Code	σ [cm]			l [cm] (1-D)			l [cm] (2-D)		
	OLSR-1	OLSR-0.25	FFT-0.25	OLSR-1	OLSR-0.25	FFT-0.25	OLSR-1	OLSR-0.25	FFT-0.25
S	1.89	0.32	0.18	17.42	3.67	0.97	29.34	3.91	0.96
SI	0.85	0.64	0.36	5.73	3.86	1.87	6.65	3.70	2.00
FYI	0.45	0.31	0.20	7.17	2.97	1.56	7.99	2.96	1.68
MYI1	1.83	0.47	0.20	17.76	4.40	1.29	22.18	4.03	1.47
MYI2	2.01	0.38	0.16	17.01	4.49	1.46	21.06	4.27	1.72

TABLE IV
COMPILATION OF SURFACE ROUGHNESS PARAMETERS EXTRACTED FROM NATURAL SEA ICE AFTER DETRENDING USING THE FFT-BASED ALGORITHM WITH A 0.25-m CUTOFF WAVELENGTH. VALUES FOR EACH SURFACE ARE AVERAGES FROM MULTIPLE LiDAR SECTIONS, WITH THE EXCEPTION OF S AND SI (SEE TABLE I)

Code	σ [cm]	l [cm] (1-D)			l [cm] (2-D)	
		Mean & Std	Min	Max	Mean & Std	ϵ_l
S	0.18	0.97 ± 0.40	0.16	2.93	0.96 ± 0.18	0.81
SI	0.36	1.87 ± 0.47	0.14	3.41	2.00 ± 0.07	0.44
FYI	0.20	1.56 ± 0.25	0.82	2.51	1.68 ± 0.21	0.70
MYI1	0.20	1.29 ± 0.35	0.31	2.92	1.47 ± 0.33	0.85
MYI2	0.16	1.46 ± 0.51	0.22	3.52	1.72 ± 0.20	0.69

natural sea ice surface, from millimeters up to tens of meters, to identify a length scale separating micro- from meso-/macroscale roughness.

In addition to collecting LiDAR data at the millimeter–centimeter scale over first-year ice in Resolute Passage in 2012, we also collected data at a lower spatial resolution (5 cm) over a much larger 100 × 100 m site to investigate geometric roughness at the snow drift scale. The size of the site was selected to be > 5 times the characteristic length of snow drifts to provide a representative sample of the surface. Since areas of a large site such as this can be "shadowed" behind objects, such as snow drifts, in the laser scanner's field-of-view, a total of four scans were collected from each corner of the site. These scans were subsequently registered to a single global coordinate system to generate a point cloud with a uniform distribution of measurements across the full site. The rms height and correlation length of topography within this site were calculated as 0.1 and 4.9 m, respectively, using the 2-D technique outlined in Section III-C1. Hereafter, all of the roughness parameters reported in this study (Tables II–VI) were derived from the smaller 1–3-m diameter sections, rather than the larger 100 × 100 m site.

We combined a 10 × 10 m section of topography with these σ and l values with a small-scale (2 × 2 m) high-resolution scan from a white ice hummock (FYI) taken a few days later, which contained microscale roughness *and* underlying mesoscale topography, into a single surface grid. With this grid, we could analyze the power spectral density of the full range of roughness elements contained within a natural sea ice

TABLE V
FORM OF SURFACE AUTOCORRELATION FOR ARTIFICIAL SEA ICE SURFACES, INCLUDING THE FRACTION OF OBSERVED 1- AND 2-D AUTOCORRELATION FUNCTIONS CONFORMING TO EITHER THE EXPONENTIAL ["EXP"; (5)] OR GAUSSIAN ["GAUSS"; (6)] MODEL AND THE MEAN AND STANDARD DEVIATION OF THE EXPONENT (n)OF A GENERALIZED POWER-LAW MODEL (7) FIT TO OBSERVED AUTOCORRELATION FUNCTIONS, ALONG WITH THE AVERAGE COEFFICIENT OF DETERMINATION (r^2) OF THE FIT

Code	1-D ACF		*n*		2-D ACF		*n*	
	Exp	Gauss	Mean & Std	r^2	Exp	Gauss	Mean & Std	r^2
BI	0.98	0.02	1.14 ± 0.12	0.96	1.00	0.00	1.02 ± 0.03	0.98
RS	1.00	0.00	1.00 ± 0.01	0.80	1.00	0.00	1.00 ± 0.00	0.75
PI-I	1.00	0.00	1.00 ± 0.02	0.65	1.00	0.00	1.00 ± 0.00	0.55
PI-II	0.99	0.01	1.01 ± 0.06	0.80	1.00	0.00	1.00 ± 0.00	0.80
PI-III	1.00	0.00	1.01 ± 0.03	0.77	1.00	0.00	1.00 ± 0.00	0.81
FF-I	0.70	0.30	1.26 ± 0.19	0.98	0.96	0.04	1.18 ± 0.06	0.99
FF-II	0.96	0.04	1.07 ± 0.12	0.94	1.00	0.00	1.01 ± 0.02	0.94
FF-III	1.00	0.00	1.03 ± 0.07	0.91	1.00	0.00	1.00 ± 0.00	0.90
FF-IV	0.93	0.07	1.09 ± 0.14	0.96	1.00	0.00	1.01 ± 0.01	0.98

TABLE VI
FORM OF SURFACE AUTOCORRELATION FOR NATURAL SEA ICE SURFACES AFTER DETRENDING (DT) USING THE FOLLOWING: 1) THE OLSR ALGORITHM WITH 1-m GRID CELLS (OLSR-1); 2) THE OLSR ALGORITHM WITH 0.25-m GRID CELLS (OLSR-0.25); AND 3) THE FFT-BASED ALGORITHM WITH A 0.25-m CUTOFF WAVELENGTH (FFT-0.25); INCLUDING THE FRACTION OF OBSERVED 1- AND 2-D AUTOCORRELATION FUNCTIONS CONFORMING TO EITHER THE EXPONENTIAL ["EXP"; (5)] OR GAUSSIAN ["GAUSS"; (6)] MODEL AND THE MEAN AND STANDARD DEVIATION OF THE EXPONENT(n) OF A GENERALIZED POWER-LAW MODEL (7) FIT TO OBSERVED AUTOCORRELATION FUNCTIONS, ALONG WITH THE AVERAGE COEFFICIENT OF DETERMINATION (r^2) OF THE FIT

Code	DT	1-D ACF		*n*		2-D ACF		*n*	
		Exp	Gauss	Mean & Std	r^2	Exp	Gauss	Mean & Std	r^2
S	(1)	0.04	0.96	1.92 ± 0.18	0.76	0.00	1.00	1.98 ± 0.06	0.79
	(2)	0.63	0.37	1.32 ± 0.31	0.92	0.53	0.47	1.35 ± 0.15	0.94
	(3)	0.94	0.06	1.08 ± 0.14	0.91	1.00	0.00	1.01 ± 0.02	0.91
SI	(1)	0.26	0.74	1.63 ± 0.33	0.89	0.24	0.76	1.53 ± 0.22	0.97
	(2)	0.33	0.67	1.58 ± 0.33	0.93	0.13	0.87	1.57 ± 0.12	0.97
	(3)	0.18	0.82	1.65 ± 0.26	0.88	0.56	0.44	1.39 ± 0.16	0.96
FYI	(1)	0.36	0.64	1.58 ± 0.36	0.91	0.52	0.48	1.33 ± 0.24	0.98
	(2)	0.50	0.50	1.40 ± 0.25	0.96	1.00	0.00	1.24 ± 0.05	0.99
	(3)	0.80	0.20	1.23 ± 0.20	0.94	1.00	0.00	1.03 ± 0.09	0.97
MYI1	(1)	0.03	0.97	1.91 ± 0.17	0.80	0.06	0.94	1.85 ± 0.18	0.90
	(2)	0.51	0.49	1.39 ± 0.29	0.93	0.62	0.38	1.39 ± 0.13	0.97
	(3)	0.80	0.20	1.23 ± 0.22	0.95	1.00	0.00	1.04 ± 0.06	0.97
MYI2	(1)	0.04	0.96	1.87 ± 0.21	0.79	0.12	0.88	1.71 ± 0.19	0.92
	(2)	0.32	0.68	1.51 ± 0.27	0.93	0.64	0.36	1.36 ± 0.06	0.97
	(3)	0.79	0.21	1.20 ± 0.21	0.93	1.00	0.00	1.01 ± 0.03	0.92

surface. The circular power spectrum can be estimated from the Fourier transform $F(f_r, f_s)$ of the rough surface $\zeta(\rho')$ using the periodogram method as [37]

$$P(f_r, f_s) = |F(f_r, f_s)|^2 + |F(f_{N-r}, f_{M-s})|^2 + |F(f_{N-r}, f_s)|^2 + |F(f_r, f_{M-s})|^2 \quad (11)$$

where

$$f_r = \frac{r}{N\Delta x} \quad f_s = \frac{s}{M\Delta y} \quad 0 < r < \frac{N}{2}, 0 < s < \frac{M}{2}. \quad (12)$$

Here, f_r and f_s are the frequency components along two coordinate axes. N and M are the number of grid cells on the x- and y-axes, respectively, and Δx and Δy are the sample spacing on the x- and y-axes, respectively. $P(f_r, f_s)$ can be interpreted as the accumulation of power spectra distributed around the four quadrants of the spectral matrix $F(f_r, f_s)$ for a given frequency $f = (f_r^2 + f_s^2)^{1/2}$ [37].

Lin *et al.* [37] demonstrated that the cutoff frequency (f_c) for removing low-frequency components (i.e., underlying topography) from a surface can be identified as a significant change in the quantity of power in the distribution of surface spectra. We conduct a basic sensitivity analysis of the grid cell size C_x of the OLSR algorithm and the cutoff frequency f_c of the FFT-based algorithm on σ and l in Section IV-B.

C. Surface Roughness Parameterization

1) Extraction of 1- and 2-D Roughness Parameters: After detrending the natural sea ice surfaces, we consider all surface grids as single-scale and extract roughness parameters in both one and two dimensions. We implement the discrete version of (1) to calculate σ for a 2-D surface grid with extent L and $N \times M$ cells. Since calculating σ from the entire surface is identical to calculating it from a series of adjacent profiles across it, we do not discriminate between 1-D and 2-D variations of the rms height.

However, for the autocorrelation function and correlation length, we can discriminate between 1-D and 2-D forms. In the 1-D case, we separately calculate the autocorrelation function for each profile across the surface in x and y dimensions (i.e., $N + M$ profiles in total) using the discrete 1-D version of (2) and then determine the normalized autocorrelation function of the surface as the average of individual functions. Likewise, we determine the surface correlation length as the mean l calculated from each individual function in x and y dimensions, using the 1-D version of (3). In contrast, in the 2-D case, we calculate a single autocorrelation function from the discrete 2-D version of (2). The 2-D correlation length is then a function describing the contour of the 2-D autocorrelation function with a normalized correlation of e^{-1}, as defined in (3). Because the 2-D form of l varies with azimuth angle, we can also evaluate the eccentricity $\in_l$ of the surface correlation using (4).

2) Form of Rough Surface Autocorrelation Function: Besides the rms height and correlation length, the form of the surface autocorrelation function (C)—whether conforming to an exponential, Gaussian, or other model—is a vital parameter in microwave scattering models. Scattering models for sea ice typically use an exponential function, since level and smooth ice surfaces have many scales of roughness, which make the correlation appear exponential-like [3]. However, we have found only one study that includes a comprehensive evaluation of C for sea ice surfaces, using a database of 1-D surface profiles [6]. Therefore, in addition to σ and l, we also calculated a number of parameters that perform the following: 1) describe whether experimental autocorrelation functions extracted from our 40 LiDAR surface sections conform to the exponential or Gaussian model and 2) characterize the exponent n of the generalized power law spectrum, given by (7), fit to the data.

We fit the exponential, Gaussian, and generalized model to each experimental C from individual 1-D profiles and also to radial profiles across the 2-D C, through artificial and natural sea ice surface sections, by minimizing the coefficient of determination (r^2) between the observations and model. From this, we obtained both 1-D and 2-D parameters for the surface autocorrelation function. Since the experimental C begins to oscillate after several correlation lengths, typically at a correlation of around zero, we restricted the model fit to a lag distance of $3l$. The entire processing chain, including data collection, preprocessing, and analysis for the extraction of surface roughness parameters, is summarized in Fig. 2.

3) Algorithm Training Using Artificial Surfaces: To ensure that the processing algorithms do not affect the roughness parameters calculated from a natural surface, we generated a series of artificial surfaces for training. We followed the method of Ogilvy and Foster [10] to generate ten random isotropic surfaces with predetermined σ and l (ranging from 0.15 to 0.35 cm and 1.0 to 3.0 cm, respectively). "Observed" roughness parameters were then calculated from each of these surfaces with our processing algorithms and compared with the original (true) parameters. The average rms error (rmse) between observed and true σ was 0.005 cm, and between observed and true l was 0.02 cm, in each case at least one order of magnitude lower than the true values of σ and l.

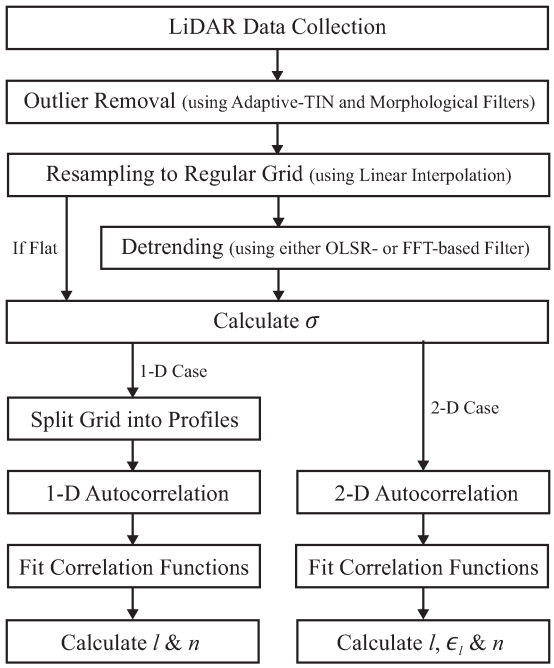

Fig. 2. Summary of the processing chain for extracting surface roughness measurements from terrestrial LiDAR data.

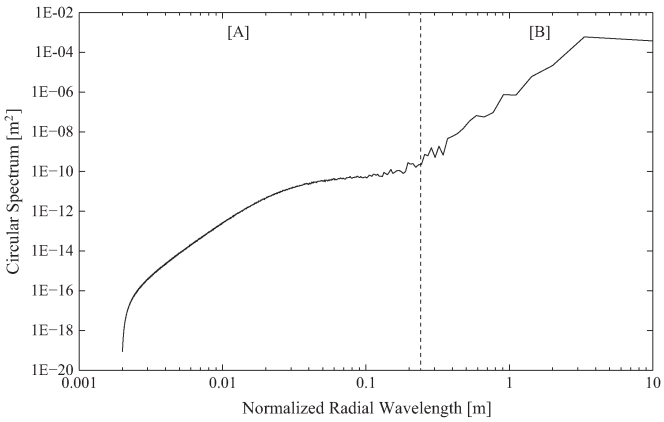

Fig. 3. Circular power spectra of combined micro- and meso-/macroscales of sea ice surface roughness. The dashed line marks a transition at approximately 0.25 m between group [A], which includes microscale roughness (assumed to interact with microwave radiation at C-band), and group [B], which includes meso- and macroscale roughness, e.g., snow drifts, deformed ice, and other elements contributing to underlying surface topography.

IV. Application and Results

A. Detrending

We assumed that the surface of young artificial ice grown in the SERF pool was uniform and flat, so the ice surface mean

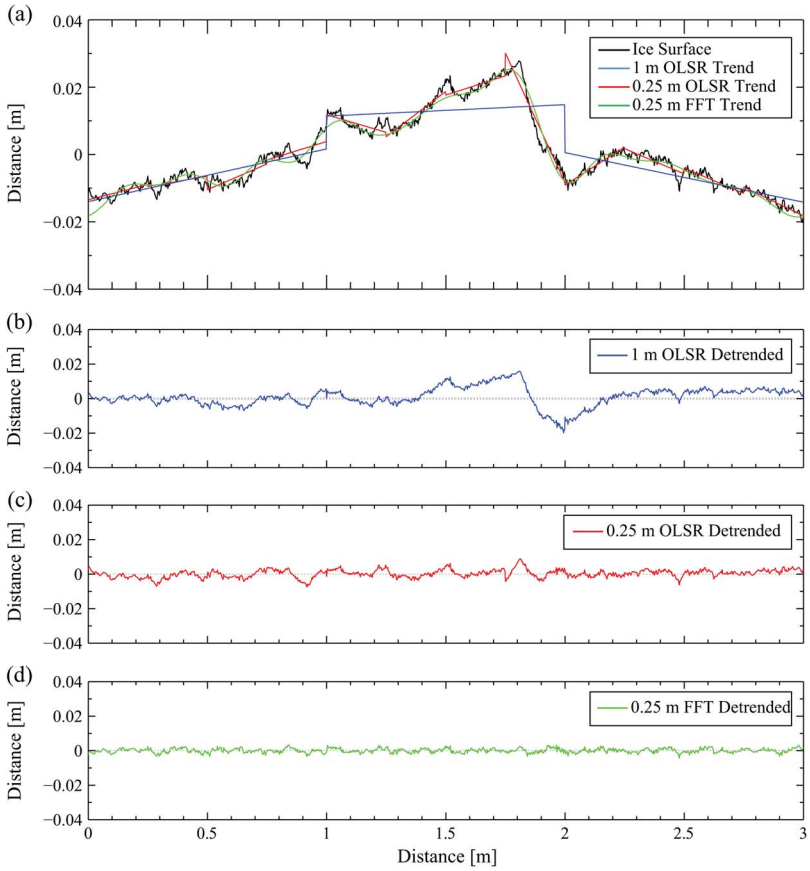

Fig. 4. Reference levels calculated through a profile across first-year sea ice (FYI subsection 5) using three detrending algorithms: OLSR with 1-m plane segments (blue), OLSR with 0.25-m plane segments (red), and FFT with a 0.25-m cutoff (green); in addition to three subsequent plots showing the height deviations from each reference level.

level corresponded to a fixed principal plane through x- and y-dimensions, parallel to the pool surface. Surface roughness of the artificial ice was therefore based only on variability in the z-dimension, and roughness parameters could be extracted directly from the original gridded data. However, the surfaces of natural sea ice (S, SI, FYI, MYI1, and MYI2) contained several superimposed scales of roughness and had to be detrended before extracting roughness parameters.

The combined circular spectra for the large-scale 100×100 m and small-scale 3×3 m LiDAR scans from first-year ice in Resolute Passage are presented in Fig. 3 as a plot of the squared amplitude of surface heights versus wavelength. Fig. 3 illustrates a significant change in power at approximately 0.25 m, corresponding to a separation between micro- and meso-/macroscales of sea ice surface roughness. Therefore, we use this value as a standard for both the grid cell size in the OLSR algorithm and the cutoff wavelength in the FFT-based algorithm to detrend the surfaces of natural ice.

An illustration of the differences between detrending with the following is presented in Fig. 4: 1) the OLSR algorithm with 1-m grid cells; 2) the OLSR algorithm with 0.25-m grid cells; and 3) the FFT algorithm with a 0.25-m cutoff wavelength. Artificial "jumps," such as those at around 1.9 m in Fig. 4(b) and (c), are introduced into detrended surfaces at the edges of plane segments using both versions of the OLSR algorithm, although detrending is clearly improved by using 0.25-m, rather than 1-m, plane segments. However, the FFT-based algorithm provides the best approximation for the surface mean line of first-year ice in Fig. 4(a) and generates flat surfaces containing only single-scale roughness elements [Fig. 4(d)].

B. Surface Roughness

One- and 2-D roughness parameters extracted from the nine artificial sea ice surfaces are presented in Table II. The rms height varies by only 0.13 cm between all ice types, in the range 0.13–0.26 cm, which lies toward the center of σ values compiled for laboratory-grown young sea ice in [33], which range from 0.02 to 0.34 cm. While σ for the pancake ice remains fairly stable at around 0.20 cm through stages I to III, σ for the frost flowers increases steadily from 0.13 to 0.26 cm from stage I to III, before dropping to 0.21 cm at stage IV. These changes in frost flower roughness are related to processes of crystal growth, brine rejection, and decimation modifying the ice surface conditions, as reported in [38], while the slight drop in σ for the pancake ice between stages I and II may be related to a "flattening" of pancake rims as the ice consolidated over time. The correlation length varies by around 2 cm, from 0.27/0.19 to 2.14/2.25 cm (1-D/2-D), between all artificial ice types, which again lies in the approximate range of l values compiled in [33], from 0.45 to 3.65 cm. l is notably different between ice types and different stages of development for the same ice type. For example, the bare ice has a 2-D l of only 0.19 cm, whereas the refrozen slush has a 2-D l of 2.25 cm,

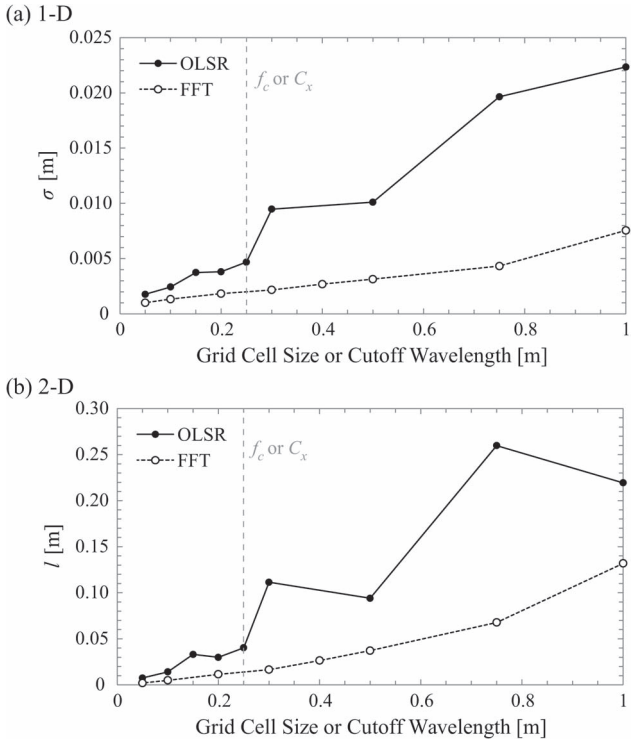

Fig. 5. Sensitivity of (a) σ and (b) 2-D l for MYI1 to variations in the grid cell size of the OLSR detrending algorithm and the cutoff wavelength of the FFT-based detrending algorithm. The grid cell size and cutoff wavelength of 0.25 m used in this study is given by the dashed gray lines.

despite both surfaces having similar σ. The pancake ice also demonstrates a significant "roughening" between stages II and III with a reduction in 2-D l from 1.36 to 0.27 cm.

Surface roughness parameters extracted from natural sea ice, after detrending with the OLSR and FFT-based algorithms, are presented in Table III. It is clear that OLSR detrending with 1-m grid cells (OLSR-1) consistently produces values for σ and l that are several times higher than OLSR detrending with 0.25-m grid cells (OLSR-0.25). Both σ and l for OLSR-1 are close to the highest values reported for first- and multiyear sea ice in [9] and [33]. However, the profile for OLSR-1 in Fig. 4(b) illustrates that background trend from a surface with high topographic relief is not fully removed with this algorithm, causing σ and l to be severely overestimated. A lack of (or inadequate) detrending, in this manner, may also explain the 1.5–4.5-cm rms heights and 4–20-cm correlation lengths measured over FYI and MYI in [6], [9], and [39]. The same is true for OLSR-0.25 but to a lesser degree, with irregular jumps between grid planes introducing false "topography" into the surface roughness [Fig. 4(c) and (b)].

Fig. 5(a) demonstrates the sensitivity of calculated σ and 1-D l to variations in the size of grid cells (C_x) in the OLSR detrending algorithm and cutoff frequency (F_c) in the FFT-based detrending algorithm, and Fig. 5(b) demonstrates the sensitivity of calculated σ and 2-D l to variations in C_x and f_c. Both σ and l are reduced significantly as C_x or F_c decreases, but their sensitivity to changes in f_c in the FFT-based algorithm is lower than their sensitivity to changes in C_x in the OLSR algorithm, especially close to the selected f_c or C_x of 0.25 m. Detrending using the FFT-based algorithm with a 0.25-m cutoff wavelength (FFT-0.25) produces the lowest values for σ and l, but these values are closer to the roughness parameters calculated in this study for artificial sea ice (Table II). Fig. 4(a) also shows that the FFT-based algorithm identifies a trend or reference level that closely follows the true ice topography. The FFT-based algorithm is clearly more suitable than the OLSR-based algorithm for detrending natural sea ice surfaces.

One- and 2-D roughness parameters extracted from the five natural sea ice surfaces using the FFT-0.25 detrending algorithm are presented in Table IV. The rms height varies by 0.20 cm between all ice types, in the range 0.16–0.36 cm, which again lies toward the center of σ values compiled for first- and multiyear sea ice in [33], which range from 0.05 to 0.89 cm. MYI is generally considered to be rougher than FYI during spring and summer, as supported by a few isolated measurements, e.g., [7] and [9], contrary to our results which suggest that FYI and MYI have similar (i.e., indistinguishable) σ around 0.2 cm. Superimposed ice has by far the highest σ of all measured sea ice types, both natural and artificial, at 0.36 cm, whereas the snow surface has a predictably low σ of 0.18 cm. The correlation length varies by around 1 cm, from 0.97/0.96 to 1.87/2.00 cm (1-D/2-D), between all natural sea ice types, which lies toward the lower end of the range of l values compiled in [33] for FYI and MYI, from 0.54 to 6.02 cm. Like σ, l is similar between first- and multiyear ice surfaces at around 1.5 cm. The superimposed ice demonstrates a relatively high l of around 2 cm, consistent with the only published measurement that we could find for superimposed ice of 2.7 cm [33], and the snow demonstrates a relatively low l of around 0.96 cm, which is almost a centimeter lower than the few reported values [39], [40].

There appears to be no bias toward either 1-D or 2-D forms of the correlation length for all sea ice types (natural and artificial), i.e., one does not consistently under- or overestimate the other. However, the average standard deviation of the 1-D form of l is 0.49 cm, which is more than twice the equivalent value for the 2-D form at 0.22 cm. Given that microwave scattering models require a single value for l that characterizes the entire surface, increasing variability in l introduces increasing variability in calculated backscatter. Indeed, this issue is emphasized when we consider the vast differences between minimum and maximum measured 1-D correlation lengths (4.34 cm on average; Tables II and IV). For instance, if a single profile is extracted from the refrozen slush surface, as if it had been collected with a laser or pin profiler, the measured correlation length could range from 0.62 to 11.12 cm (Table II).

A fraction of this variability in l is caused by surface anisotropy, and this is captured by the eccentricity of the 2-D correlation length. Of the artificial ice surfaces, the bare ice is near isotropic, but the refrozen slush, pancake ice, and especially frost flowers are clearly anisotropic (Table II). In the case of the pancake ice, this may have been caused by the linear rims [see Fig. 1(c)], whereas after examining the frost flowers, it appears that surface winds may have arranged the crystal structures into a linear pattern that was subsequently measured with the laser scanner. Of the natural ice surfaces, the superimposed ice is close to isotropic, but the first- and multiyear ice and snow are anisotropic. These results are consistent with the

results of Manninen [6], who found that sea ice and especially snow regularly showed strong anisotropy.

C. Form of Rough Surface Autocorrelation Function

One- and 2-D parameters describing the form of autocorrelation for the nine artificial sea ice surfaces are presented in Table V. Profiles across all nine surfaces largely conform to the exponential function, in both 1-D and 2-D forms, with the exception of the 1-D form for frost flowers stage I (FF-I), which demonstrates a 70%–30% split between exponential and Gaussian functions. The exponent of the x-exponential function n is close to 1 across all nine surfaces, again with the exception of FF-I, which has 1-D and 2-D n values of 1.26 and 1.18, respectively, and generally, the goodness-of-fit (r^2) is high for profiles fit to the x-exponential function. The r^2 values for 2-D x-exponential functions are all above 0.75, excluding pancake ice stage I (PI-I), which has an r^2 of 0.55 and does not demonstrate a strong agreement with either the exponential or Gaussian function. It is possible that the rims around individual consolidated pancakes—defined and a few centimeters high at stage I, but increasingly flattened thereafter—distorted the correlation function (likely exponential, given the form of C for PI-II and PI-III) at this early stage.

Parameters describing the form of autocorrelation for the five natural sea ice surfaces, after detrending with the OLSR and FFT-based algorithms, are presented in Table VI. Four of the surfaces, namely, S, FYI, MY1, and MYI2, demonstrate enormous variation in n when detrending with the OLSR-1, OLSR-0.25, and FFT-0.25 algorithms. The least successful algorithm, OLSR-1, generates surfaces that principally conform to the Gaussian correlation function, producing minimum 1-D and 2-D n values of 1.91 and 1.85, respectively, for MYI1, due to the widening of the observed autocorrelation function and diminished influence of the smallest scale surface roughness elements. The OLSR-0.25 algorithm generates surfaces somewhere between exponential and Gaussian. However, the FFT-0.25 algorithm, which is shown in Fig. 4(a) to generate the best reference level through natural sea ice topography, produces surfaces largely conforming to the exponential correlation function, with maximum 1-D and 2-D n values of 1.23 and 1.04, respectively, between these four surface types. This variation in modeled C with the choice of detrending algorithm reveals the importance of both performing detrending in the first place and then selecting a sophisticated enough technique, such as FFT-based filtering.

The exception to this trend of a Gaussian-to-exponential shift with improving detrending is the superimposed ice (SI) surface, which remains primarily Gaussian as the detrending algorithm is changed from OLSR-1 through to FFT-0.25. This indicates that, of all natural and artificial sea ice surface types, superimposed ice, exclusively, has a Gaussian autocorrelation function. This observation is in agreement with the results of Manninen [6] who measured hundreds of profiles of small-scale roughness across Baltic sea ice and found that only around 10% conformed to the Gaussian, rather than exponential, correlation function. The goodness-of-fit (r^2) for profiles fit to the x-exponential function is high for all surfaces, detrended with

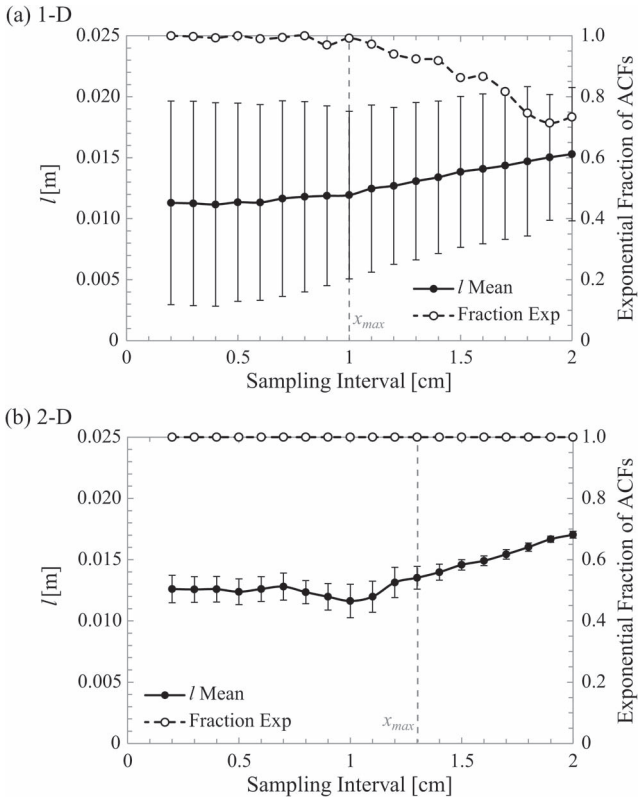

Fig. 6. Change in the (a) 1-D and (b) 2-D mean and standard deviation correlation length (bold points and bold line) and exponential fraction of curves fit to experimental autocorrelation functions (hollow points and dashed line) for pancake ice stage 1 (PI-I) subsection 1 as the sampling interval is varied. The threshold maximum sampling interval $\Delta x_{\max}$ is given by a dashed gray line.

all three algorithms, with r^2 values for 2-D x-exponential functions above 0.91 after detrending with FFT-0.25 for all five surfaces. However, the average 1-D standard deviation of n for both natural and artificial sea ice surfaces is noticeably higher than the equivalent average 2-D standard deviation (after detrending with FFT-0.25: 0.21 versus 0.07; Tables V and VI). Like the vast differences in minimum and maximum measured 1-D correlation lengths (discussed previously), the much wider variation in 1-D rather than 2-D n illustrates the lack of precision associated with using a 1-D approach, e.g., laser or pin profiling, to measure surface roughness.

D. Sensitivity of Surface Roughness Parameters to the Sampling Interval and Extent

To examine the dependence of roughness parameters σ, l, and C on the sampling interval Δx and extent L, we performed two simple experiments on select ice surface sections, including bare congelation ice (BI) subsection 1 and pancake ice stage I (PI-I) subsection 1. In the first, we reduced the spatial resolution of the grid, resampled from original LiDAR points, at regular intervals of 1 mm from the highest resolution of 2 mm down to 20 mm, and calculated 1-D and 2-D surface roughness parameters at each iteration. For both PI-I and BI, σ barely changes as the grid is downsampled, but l and the form of C vary dramatically and quite differently between the two surface types (Figs. 6 and 7). For both surfaces, l increases, and the fraction of observed C conforming to the exponential model

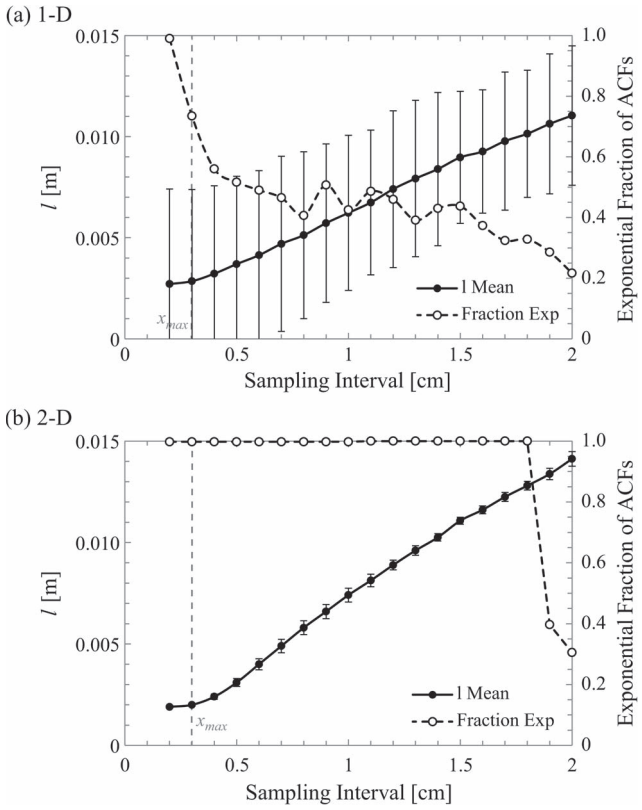

Fig. 7. Change in the (a) 1-D and (b) 2-D mean and standard deviation correlation length (bold points and bold line) and exponential fraction of curves fit to experimental autocorrelation functions (hollow points and dashed line) for bare ice (BI) subsection 1 as the sampling interval is varied. The threshold maximum sampling interval $\Delta x_{\max}$ is given by a dashed gray line.

decreases as Δx is reduced, but the critical maximum sampling threshold $\Delta x_{\max}$, above which l increases, varies between the two surfaces. To estimate $\Delta x_{\max}$, we calculate the relative percentage change of l with respect to l at the highest grid resolution of 2 mm

$$\Delta l_{\%} = \frac{(l - l_{2\mathrm{mm}})}{l_{2\mathrm{mm}}}.100 \tag{13}$$

as the grid is downsampled. $\Delta x_{\max}$ is then identified as the lowest resolution, where $\Delta l_{\%} \leq 10\%$.

Whereas l remains almost constant from 2 mm up to $\Delta x_{\max}$ of 10 mm (1-D) and 13 mm (2-D) for the pancake ice (Fig. 6), it rapidly increases after $\Delta x_{\max}$ of 3 mm in both 1-D and 2-D cases for the bare ice (Fig. 7). The fraction of exponential C also decreases more rapidly with decreasing Δx for the bare ice rather than pancake ice. This can be explained by the differences in measured l between the two surface types, which, using the 2-D measurements from Table II, show that pancake ice has a correlation length of 1.27 cm, almost an order of magnitude higher than the bare ice at 0.19 cm. A sampling interval of 2 mm would provide over six data points within one correlation length of PI-I but only around one data point within one correlation length of BI, so any further reduction in Δx has a greater impact on measured l and C from BI than PI-I.

In the second experiment, we kept the grid resolution at 2 mm, but gradually reduced the sampling extent from the full 3 × 3 m section down to 1.5 × 1.5 m and then to 1 × 1 m and so on to only 5 × 5 cm, and calculated 1-D and 2-D surface roughness parameters at each iteration. At 3-m extent, a single set of parameters was calculated for the section, but at subsequent iterations, the roughness parameters were calculated as an average of subsections, e.g., 4 × 1.5 m sections or 9 × 1 m sections, within the larger 3-m section. We observe that σ does not change as L decreases, but for both surfaces, l decreases in a similar manner as L drops, and the result for PI-I is illustrated in Fig. 8. To estimate the critical minimum threshold for the sampling extent $L_{\min}$, we calculate the relative percentage change of l as L decreases, in the same manner as (13), but with respect to l at the largest 3 × 3 m extent. Again, we identify $L_{\min}$ as the largest extent where $\Delta l_{\%} \leq 10\%$. For the 1-D measurements, l decreases exponentially from 3-m extent, and even the second-largest extent (1.5 m) provides $\Delta l_{\%} > 10\%$, indicating that $L_{\min} > 1.5$ m [Fig. 8(a)]. In contrast, for the 2-D measurements, l only starts to decrease significantly at $L_{\min}$ under 0.25 m [Fig. 8(b)].

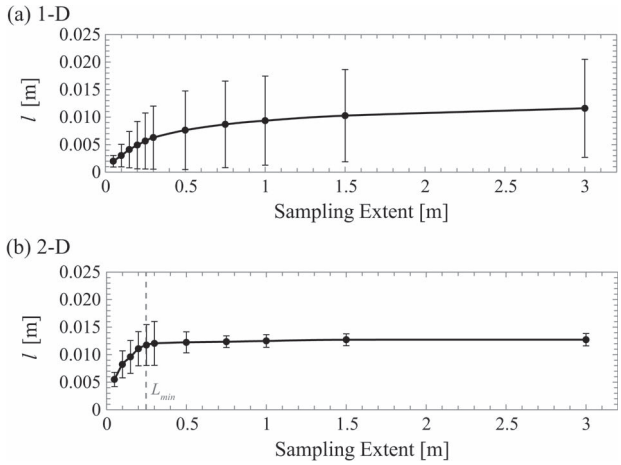

Fig. 8. Change in the (a) 1-D and (b) 2-D mean and standard deviation correlation length for pancake ice stage 1 (PI-I) subsection 1 as the sampling extent is varied. The threshold minimum sampling extent $L_{\min}$ is given by a dashed gray line in the 2-D case (b), but since $L_{\min} > 1.5$ m in the 1-D case (a), it is left unmarked.

A noticeable result from both of these experiments is that the standard deviation of l is typically several orders of magnitude higher using the 1-D approach rather than the 2-D approach, even as the two sampling parameters are varied (Figs. 6–8). We have already demonstrated that the average standard deviation of 1-D correlation lengths measured over sea ice surfaces in this study is more than twice equivalent 2-D correlation lengths (see Section IV-B). Both results support the argument that the 2-D approach is considerably more precise than the 1-D approach and is therefore able to characterize the surface correlation length as a single-scale stationary process for microwave scattering models, which the 1-D approach cannot do.

E. Relationship Between σ and l

Fig. 9 illustrates the relationship between the rms height and 2-D correlation length of measurements acquired over 14 sea ice surface types in this study, in the context of literature values

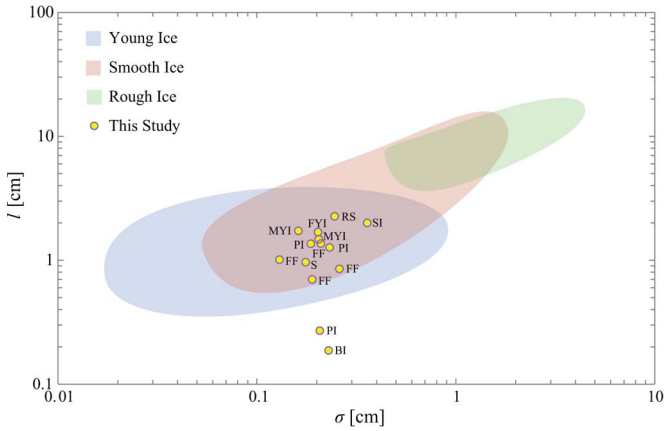

Fig. 9. Comparison between the rms height and two-dimensional correlation length of sea ice surfaces examined in this study. Literature values, grouped as young ice (obtained in the laboratory or field), smooth ice (FYI or MYI, obtained in the field only), and rough ice (FYI or MYI, obtained in the field only), are presented as shaded zones in the background.

obtained from [3], [6], [9], [33], [39]–[43]. Although the literature values appear to demonstrate a weak linear trend of increasing l with increasing σ, our measurements suggest that no such relationship exists. Our lowest measured value for σ, over FF-I, has a moderate corresponding l, and similarly, our lowest measured value for l, over BI, has a moderate corresponding σ, although one of our highest measured values for σ, over SI, also has a particularly high l. These results indicate that there is no clear dependence of l on σ or vice versa, which suggests that the geophysical processes controlling surface roughness as an ice sheet forms and evolves can *independently* modify σ or l, not necessarily both simultaneously. This contrasts the result of Manninen [6], who found an exponential relationship between l and σ, obtained from hundreds of short (0.1–1 m) 1-D profiles recorded over Baltic sea ice. However, we believe that their relationship characterizes the sensitivity of σ and l to the sampling extent and fractal nature of ice surface roughness within a small area, which is especially significant for a 1-D approach [Fig. 8(a)], and is shown by our results to break down as L exceeds $L_{\min}$ (Section IV-D).

V. Discussion

A. Potential Sources of Error

Terrestrial laser scanning delivers several advantages over conventional techniques for measuring surface roughness at radar-observable scales. However, it is not without limitation. Leica C10 is limited by the diameter of the laser footprint and, even at the lowest ranges, cannot resolve elements of the target surface that are smaller than $\sim$1 mm. Snow and ice grains are often smaller than 1 mm [41]; however, an electromagnetic wave at C-band does not interact with surface roughness at this scale [12]. At a scanning range of approximately 20 m, $D_{f_{\text{across}}}$ of Leica C10 exceeds 5 mm, which is approximately the criteria of Ulaby [12] for C-band. Above this range, consecutive samples may become correlated if $\Delta < 0.859\delta$ [32]. In other words, the Gaussian peaks of adjacent laser pulses may cross, and the scanner will not resolve elements of the surface between these samples.

If the target surface is inclined with respect to the scanning origin ($\theta > 0$), $D_{f_{\text{along}}}$ will also be larger than $D_{f_{\text{across}}}$. The laser footprint will become increasingly elliptical in the along-track direction as θ rises. θ can be reduced by either elevating the scanner to a greater height above the target surface or restricting the range. Terrestrial laser scanners have a limited field-of-view in the zenith angles, including Leica C10, which is constrained to $\theta > 45^\circ$. However, we have demonstrated that, by restricting the maximum range of C10 to approximately 10 m, at a mounting height of 3 m, x_{opt} in the along-track direction is at most 6.8 mm for a scan with a maximum range of 10 m. If the scan were restricted to a maximum range of 8 m, maximum x_{opt} along-track would fall to 4.4 mm.

When the scanner operates at a low incidence angle, it also preferentially samples high points of the local surface topography and slopes with an aspect toward the scanner. Consequently, the observed anisotropy in surface roughness (Tables II and IV) may partially be an artifact of the scanning perspective. The anisotropy cannot entirely be attributed to the scanning perspective because the axis of highest correlation (i.e., the a-axis of the 1/e contour of 2-D C) was rarely oriented parallel or perpendicular to the scanning origin and varied considerably between scans of different ice surfaces (data not shown). Besides this, satellite radars are intentionally "looking" at the ice from an oblique perspective in the same way the terrestrial LiDAR system is.

As explained in Section III-A, the laser may penetrate into the snow or sea ice surface for several millimeter, and the pulse return will therefore be a time-spread combination of surface and volume backscatter. Past observations indicate that green light is primarily backscattered by surface specular reflection from most of the snow and ice types measured in this study [29], [30]. However, observations have also shown that light reflected from cold dry snow has a strong volume scattering component [29]. A terrestrial LiDAR sensor with a green laser may not be able to accurately measure the surface roughness of dry snow, although for radar remote sensing at C-band, the radar wave penetrates into the dry snowpack, and the snow surface roughness is inconsequential [33]. In spite of this, the extinction coefficients for sea ice are larger at 1000 nm wavelength [near infrared (NIR)] than at 500 nm (green) [28], which means that a NIR laser would penetrate into the snow or ice to a shallower depth than a green laser. A LiDAR sensor with a NIR laser is therefore advantageous over a system with a green laser (such as Leica C10) for measuring snow and sea ice surface roughness.

B. Implications for Microwave Scattering From Sea Ice

The small perturbation model (SPM) has been widely used to simulate the scattering of electromagnetic waves from a rough interface separating two media [3]. In the SPM, besides the frequency, incidence angle, polarization, and dielectric properties of the media, the backscattering coefficient strongly depends on the rms height, correlation length, and correlation function, which together characterize the rough surface. Our results have

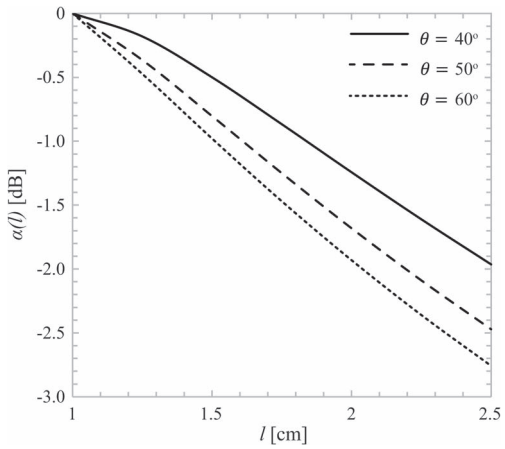

Fig. 10. Sensitivity of $\alpha(l)$ (relative change in σ^0) to variations in l, for the exponential correlation function, at 40°, 50°, and 60° incidence angles.

shown that the technique used to measure surface roughness in the field and the procedures used to postprocess the field data can affect the derived σ, l, and C considerably. One-dimensional profiling versus 2-D surface-based measurement affects the precision of σ and l. Insufficient detrending causes σ and l to be overestimated and C to be incorrectly classified. Two-dimensional measurements allow l to be characterized as a function of azimuth angle φ for sea ice surfaces that are typically anisotropic.

To demonstrate the sensitivity of the backscatter to these factors, we have used SPM theory to calculate the relative change in HH or VV backscatter σ^0 associated with a minor change in l that might be caused by errors in the field measurement technique, inhomogeneity of the surface, or surface anisotropy. The sensor parameters (frequency, polarization, and incidence angle) and surface parameters (permittivity and rms height) are fixed. Then, the relative change in σ^0 associated with a change in l for the exponential correlation function is [3]

$$a(l) = \frac{\sigma^0(l)}{\sigma^0(l_0)} = \left(\frac{l^2}{l_0^2}\right)\left[\frac{1+(2kl_0\sin\theta)^2}{1+(2kl\sin\theta)^2}\right]^{1.5} \tag{14}$$

where k is the wavenumber ($k = 2\pi/\lambda = 114\ \mathrm{m}^{-1}$ at C-band), θ is the incidence angle, and l_0 is a reference correlation length of 1 cm, corresponding to approximately the lowest observed value in this study. The relative change in σ^0 for a 1.5-cm change in l is between 2 and 3 dB, increasing at higher incidence angles (Fig. 10).

It is not only the millimeter–centimeter-scale roughness that affects the radar backscatter but also the larger (meter) scale topographic roughness of the sea ice surface. SPM theory can be extended to a case where the small-scale roughness is modulated by large-scale topography. In this situation, the large-scale topography is characterized as a distribution of surface slopes [12]. The technique that we have developed in this study could be scaled up to examine the 2-D large-scale roughness of sea ice. However, airborne LiDAR would be a more suitable tool than terrestrial LiDAR for measuring roughness at this scale [44].

VI. Conclusion

A technique has been developed for calculating surface roughness parameters from 3-D elevation data acquired with a terrestrial LiDAR system. The technique includes several steps, involving the following: 1) raw data preprocessing; 2) resampling of data to a regular grid; 3) detrending (where necessary); and 4) 2-D autocorrelation, to characterize the surface rms height, correlation length, and autocorrelation function. We have introduced a pair of 2-D detrending algorithms that can be used to remove macroscale topography from a surface section and evaluated their capacity to detrend natural sea ice surfaces, leaving a single scale of roughness suitable for extracting roughness parameters. We have then presented surface roughness parameters for various types of sea ice, some at different stages of physical development, calculated using this technique.

Our main conclusions are as follows.

1) The terrestrial LiDAR can be used to measure surface roughness at millimeter–centimeter scale, provided that the LiDAR system is elevated to a height of 2.5–3 m above the surface and the range is restricted to approximately 10 m.
2) The terrestrial LiDAR is most suitable for measuring the roughness of snow and sea ice types which demonstrate strong surface specular reflection at visible or NIR wavelengths, including glazed snow, melting white ice, blue ice, pancake ice, frost flowers, and young congelation ice. More research is required to evaluate the suitability over dry snow, where volume scattering may bias the ranging estimate of the sensor.
3) The 2-D approach for parameterizing surface roughness is considerably more precise than the traditional 1-D profiling approach and is therefore able to characterize a surface while satisfying an underlying assumption of stationarity, required by most backscatter models, which the 1-D generally cannot do.
4) An absence of, or inadequate, detrending retains macro- and/or mesoscale topography in surface roughness calculations, leading to an overestimation of σ and l, and, typically, also erroneously classifies the surface correlation function as Gaussian rather than exponential. Of the 14 sea ice surface types examined in this study, 13, including first- and multiyear ice, could be characterized with the exponential function and only one with the Gaussian.
5) The critical maximum sampling interval and minimum sampling extent are dictated by the surface correlation length. The correlation length of pancake ice, typical of most sea ice surfaces at around 1.5 cm, provides $\Delta x_{\max} \sim 1$ cm and $L_{\min} \sim 30$ cm, but the correlation length of bare congelation ice, at around 0.3 cm, provides similar $x_{\max}$ to l of approximately 0.2 cm. We have demonstrated that the 2-D sampling approach increases $\Delta x_{\max}$ and decreases $L_{\min}$, but clearly when $\Delta x \to l$, e.g., for bare ice when $\Delta x = 2$ mm, the sampling interval is inadequate for characterizing the correlation function.
6) The correlation functions of most natural and artificial sea ice surfaces examined in this study, including first- and multiyear ice, are strongly anisotropic, indicating that a

sea ice surface cannot generally be treated as an isotropic scattering interface in backscatter models (as is typically the case). Rather, the correlation length should vary as a function of the azimuth angle, so that backscatter depends on both the radar incidence angle and the azimuth angle of surface correlation with respect to the incident beam [3].

7) Our results demonstrate that there is no fundamental relationship between σ and l at the centimeter scale for sea ice surfaces. We speculate that earlier studies indicating such a relationship have actually characterized the fractal nature of surface roughness within a small area, i.e., the association between the rms height, correlation length, and sampling extent when $L < L_{\min}$, rather than a more general relationship.

ACKNOWLEDGMENT

The authors would like to thank the crew of the CCGS Amundsen Icebreaker and research teams involved with the 2011 ArcticNet/IORVL project and 2012 Arctic-ICE and SERF projects, and A. Chaulk for her assistance at the SERF facility. This paper is dedicated to Dr. K. Hochheim who lost his life in September 2013.

REFERENCES

[1] D. G. Barber, "Microwave remote sensing, sea ice and Arctic climate," *Phys. Can.*, vol. 61, pp. 105–111, Sep. 2005.

[2] D. Winebrenner *et al.*, "Microwave sea ice signature modeling," in *Microwave Remote Sensing of Sea Ice*, vol. 68, F. Carsey, Ed. Washington, DC, USA: American Geophysical Union, 1992, pp. 137–175.

[3] A. K. Fung, *Microwave Scattering and Emission Models and Their Applications*. Norwood, MA, USA: Artech House, 1994.

[4] J. Ogilvy, *Theory of Wave Scattering From Random Rough Surfaces*. London, U.K.: Institute of Psychiatry, 1991.

[5] N. E. Verhoest *et al.*, "On the soil roughness parameterization problem in soil moisture retrieval of bare surfaces from synthetic aperture radar," *Sensors*, vol. 8, no. 7, pp. 4213–4248, 2008.

[6] A. Manninen, "Surface roughness of Baltic sea ice," *J. Geophys. Res.*, vol. 102, no. C1, pp. 1119–1139, Jan. 1997.

[7] J. Paterson, B. Brisco, S. Argus, and G. Jones, "*In situ* measurements of micro-scale surface roughness of sea ice," *Arctic*, vol. 44, no. 1, pp. 140–146, 1991.

[8] L. Tsang, J. Kong, and K.-H. Ding, *Scattering of Electromagnetic Waves: Theories and Applications*. New York, NY, USA: Wiley, 2000.

[9] M. Drinkwater, "LIMEX '87 ice surface characteristics: Implications for C-band SAR backscatter signatures," *IEEE Trans. Geosci. Remote Sens.*, vol. 27, no. 5, pp. 501–513, Sep. 1989.

[10] J. Ogilvy and J. Foster, "Rough surfaces: Gaussian or exponential statistics?" *J. Phys. D, Appl. Phys.*, vol. 22, no. 9, pp. 1234–1251, Sep. 1989.

[11] Y. Oh and Y. Kay, "Condition for precise measurement of soil surface roughness," *IEEE Trans. Geosci. Remote Sens.*, vol. 36, no. 2, pp. 691–695, Mar. 1998.

[12] F. Ulaby, R. Moore, and A. Fung, *Microwave Remote Sensing: Active and Passive*, vol. II. Boston, MA, USA: Artech House, 1982.

[13] M. Nishimoto, "Characteristics of rough surface parameters estimated from measured surface profile of finite length," in *Proc. IGARSS*, Honolulu, HI, USA, Jul. 2010, pp. 4436–4439.

[14] F. Mattia and T. L. Toan, "Backscattering properties of multi-scale rough surfaces," *J. Electromagn. Waves Appl.*, vol. 13, no. 4, pp. 491–526, 1999.

[15] T. Mathia, P. Pawlus, and M. Wieczorowski, "Recent trends in surface metrology," *Wear*, vol. 271, no. 3/4, pp. 494–508, Jun. 2011.

[16] F. Mattia *et al.*, "A comparison between soil roughness statistics used in surface scattering models derived from mechanical and laser profilers," *IEEE Trans. Geosci. Remote Sens.*, vol. 41, no. 7, pp. 1659–1671, Jul. 2003.

[17] R. Bryant *et al.*, "Measuring surface roughness height to parameterize radar backscatter models for retrieval of surface soil moisture," *IEEE Trans. Geosci. Remote Sens.*, vol. 4, no. 1, pp. 137–141, Jan. 2007.

[18] W. Jester and A. Klik, "Soil surface roughness measurement—Methods, applicability, and surface representation," *Catena*, vol. 64, no. 2/3, pp. 174–192, Dec. 2005.

[19] C. Manes *et al.*, "Statistical properties of fresh snow roughness," *Water Resources Res.*, vol. 44, no. 11, p. W11407, Nov. 2008.

[20] M. Callens, N. Verhoest, and M. Davidson, "Parameterization of tillage-induced single-scale soil roughness from 4-m profiles," *IEEE Trans. Geosci. Remote Sens.*, vol. 44, no. 4, pp. 878–887, Apr. 2006.

[21] M. Gupta, D. G. Barber, R. K. Scharien, and D. Isleifson, "Detection and classification of surface roughness in an Arctic marginal sea ice zone," *Hydrol. Process.*, vol. 28, no. 3, pp. 599–609, Jan. 2014.

[22] W. Warner, "Mapping a three-dimensional soil surface with handheld 35 mm photography," *Soil Tillage Res.*, vol. 34, no. 3, pp. 187–197, Jun. 1995.

[23] P.-C. Gutierrez, J. Martinez-Fernandez, N. Sanchez, and J. Álvarez-Mozos, "Modeling of soil roughness using terrestrial laser scanner for soil moisture retrieval," in *Proc. IGARSS*, Barcelona, Spain, 2007, pp. 1877–1880.

[24] R. Pollyea and J. Fairley, "Estimating surface roughness of terrestrial laser scan data using orthogonal distance regression," *Geology*, vol. 39, no. 7, pp. 623–626, 2011.

[25] C. Petrich and H. Eicken, "Growth, structure and properties of Sea ice," in *Sea Ice*. Oxford, U.K.: Blackwell, 2010, pp. 23–78.

[26] M. Granskog, T. Vihma, R. Pirazzini, and B. Cheng, "Superimposed ice formation and surface energy fluxes on sea ice during the spring melt-freeze period in the Baltic Sea," *J. Glaciology*, vol. 52, no. 176, pp. 119–127, 2006.

[27] G. Maykut and T. Grenfell, "The spectral distribution of light beneath first-year sea ice in the Arctic Ocean," *Limnol. Oceanogr.*, vol. 20, no. 4, pp. 554–563, 1975.

[28] D. Perovich, *The Optical Properties of Sea Ice*. Hanover, NH, USA: US Office of Naval Research, 1996.

[29] D. Perovich, "Light reflection from sea ice during the onset of melt," *J. Geophys. Res.*, vol. 99, no. C2, pp. 3351–3359, Feb. 1994.

[30] D. Perovich, "Observations of the polarization of light reflected from sea ice," *J. Geophys. Res.*, vol. 103, no. C3, pp. 5563–5575, Mar. 1998.

[31] E. Baltsavias, "Airborne laser scanning: Basic relations and formulas," *ISPRS J. Photogramm. Remote Sens.*, vol. 54, no. 2/3, pp. 199–214, Jul. 1999.

[32] D. Licthi and S. Jamtsho, "Angular resolution of terrestrial laser scanners," *Photogramm. Rec.*, vol. 21, no. 114, pp. 141–160, Jun. 2006.

[33] R. G. Onstott, "5. SAR and scatterometer signatures of sea ice," in *Microwave Remote Sensing of Sea Ice*, F. D. Carsey, Ed. Washington, DC, USA: American Geophysical Union, 1992, pp. 73–104.

[34] G. Petrie and C. K. Toth, *Terrestrial Laser Scanners*, J. Shan and C. K. Toth, Eds. Boca Raton, FL, USA: CRC Press, 2009, pp. 87–127.

[35] G. Vosselman, "Slope based filtering of laser altimetry data," *Int. Archives Photogramm. Remote Sens.*, vol. 33, pp. 935–942, 2000.

[36] P. Axelsson, "DEM generation from laser scanner data using adaptive TIN models," *Int. Archives Photogramm. Remote Sens.*, vol. 33, pp. 110–117, 2000.

[37] T. Lin, L. Blunt, and K. Stout, "Determination of proper frequency bandwidth for 3D topography measurement using spectral analysis. Part I: Isotropic surfaces," *Wear*, vol. 166, no. 2, pp. 221–232, Jul. 1993.

[38] D. Isleifson *et al.*, "A study on the C-band polarimetric scattering and physical characteristics of frost flowers on experimental sea ice," *IEEE Trans. Geosci. Remote Sens.*, vol. 52, no. 3, pp. 1787–1798, Mar. 2014.

[39] L. Farmer *et al.*, *Beaufort Sea Ice—1*. Hanover, NH, USA: Naval Oceanographic and Atmospheric Research Laboratory, 1991.

[40] S. Nghiem, R. Kwok, S. Yueh, and M. Drinkwater, "Polarimetric signatures of sea ice 2. Experimental observations," *J. Geophys. Res.*, vol. 100, no. C7, pp. 13681–13698, Jul. 1995.

[41] C. Swift *et al.*, "Laboratory investigations of the electromagnetic properties of artificial sea ice," in *Microwave Remote Sensing of Sea Ice*. Washington, DC, USA: American Geophysical Union, 1992, pp. 177–200.

[42] S. G. Beaven, S. P. Gogineni, A. Gow, A. Lohanick, and K. Jezek, Radar Backscatter Measurements From Simulated Sea Ice During CRRELEX'90 1993.

[43] E. Nassar, "Numerical and Experimental Studies of Electromagnetic Scattering From Sea Ice," M.S. Thesis, Ohio State Univ., Columbus, OH, USA, 1997.

[44] M. Belmonte-Rivas, J. Maslanik, J. Sonntag, and P. Axelrad, "Sea ice roughness from airborne LiDAR profiles," *IEEE Trans. Geosci. Remote Sens.*, vol. 44, no. 11, pp. 3032–3037, Nov. 2006.

[45] P. U. A. Rieger, "Resolving range ambiguities in high-repetition rate airborne LiDAR applications," in *Proc. SPIE Proc.*, 2011.

Jack C. Landy received the B.S. degree in physical geography and the M.S. degree in remote sensing from the University of Durham, Durham, U.K., in 2009 and 2011, respectively. He has been working toward the Ph.D. degree in Arctic system science at the University of Manitoba, Winnipeg, MB, Canada, since 2011.

In his Master's degree, he studied the application of airborne light detection and ranging (LiDAR) for generating digital terrain models under forest canopy, with a focus on remote archaeological prospecting. In his doctoral degree, he is using terrestrial LiDAR to study thermodynamic processes operating at the surface of melting sea ice and develop new techniques for characterizing snow and sea ice surface roughness. His primary research interest is in remote sensing, particularly the use of LiDAR technology for understanding environmental processes.

Dustin Isleifson received the B.Sc. degree in electrical engineering (with distinction) and the Ph.D. degree in electrical and computer engineering from the University of Manitoba, Winnipeg, MB, Canada, in 2005 and 2011, respectively.

From 2011 to 2013, he was a Research Associate working in a joint appointment between the Department of Electrical and Computer Engineering and the Centre for Earth Observation Science, University of Manitoba. He is currently an Electrical Engineer with Magellan Aerospace, where his work is focused on the development and provision of the Radarsat Constellation Mission. He has conducted research in the Canadian Arctic through ArcticNet and the Circumpolar Flaw Lead System Study (CFL). He held a Canadian NSERC Canada Graduate Scholarship CGS-M in 2006 and held an NSERC Canada Graduate Scholarship CGS-D3 during his Ph.D. studies. His research interests are in the areas of microwave remote sensing and Arctic science.

Alexander S. Komarov (S'10) was born in Barnaul, Russia, in 1986. He received the B.Sc. (Hons.) degree in radiophysics and electronics and the M.Sc. (Hons.) degree in physics from Altai State University, Barnaul, in 2006 and 2008, respectively. He has been working toward the Ph.D. degree in electrical engineering at the University of Manitoba, Winnipeg, MB, Canada, since 2010.

His Master's research focused on passive microwave remote sensing of soil moisture, which was partially conducted at the Canada Centre for Remote Sensing, Natural Resources Canada, Ottawa, ON, Canada. From 2008 to 2010, he was a Physical Scientist and then Contractor with the Canadian Ice Service and the Meteorological Service of Canada, Environment Canada, Ottawa. He has held a Natural Sciences and Engineering Research Council of Canada Alexander Graham Bell Canada Graduate Scholarship (CGS-D3) and a Manitoba Graduate Scholarship. His current research interests include sea ice motion tracking from SAR imagery, ocean surface wind speed retrieval from SAR, and measurements and modeling of electromagnetic wave scattering from sea ice.

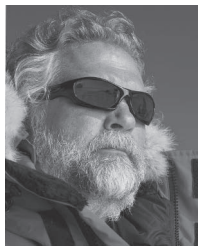

David G. Barber received the Bachelor's and Master's degrees from the University of Manitoba, Winnipeg, MB, Canada, in 1981 and 1987, respectively, and the Ph.D. degree from the University of Waterloo, Waterloo, ON, Canada, in 1992.

He was appointed to a faculty position at the University of Manitoba in 1993 and received a Canada Research Chair in Arctic System Science in 2002. He is currently the Director of the Centre for Earth Observation Science and the Associate Dean (Research) of the CHR Faculty of Environment, Earth and Resources.